

Accepted for publication in *The Astrophysical Journal* 9/16/96

Ultraviolet Emission Line Ratios of Cataclysmic Variables¹

Christopher W. Mauche

Lawrence Livermore National Laboratory,
L-41, P.O. Box 808, Livermore, CA 94550;
mauche@cygnus.llnl.gov

Y. Paul Lee²

Lawrence Livermore National Laboratory, Livermore, CA 94550 and
Department of Physics, University of California, Davis, CA 95616

and

Timothy R. Kallman

Laboratory for High Energy Astrophysics,
NASA/Goddard Space Flight Center, Code 665, Greenbelt, MD 20771;
tim@xstar.gsfc.nasa.gov

¹Based on observations with the *International Ultraviolet Explorer* satellite, which is sponsored and operated by the National Aeronautics and Space Administration, the Science Research Council of the United Kingdom, and the European Space Agency.

²Present address: Space Telescope Science Institute, 3700 San Martin Drive, Baltimore, MD 21218; plee@stsci.edu

ABSTRACT

We present a statistical analysis of the ultraviolet emission lines of cataclysmic variables (CVs) based on ≈ 430 ultraviolet spectra of 20 sources extracted from the *International Ultraviolet Explorer* Uniform Low Dispersion Archive. These spectra are used to measure the emission line fluxes of N V, Si IV, C IV, and He II and to construct diagnostic flux ratio diagrams. We investigate the flux ratio parameter space populated by individual CVs and by various CV subclasses (e.g., AM Her stars, DQ Her stars, dwarf novae, nova-like variables). For most systems, these ratios are clustered within a range of ~ 1 decade for $\log \text{Si IV/C IV} \approx -0.5$ and $\log \text{He II/C IV} \approx -1.0$ and ~ 1.5 decades for $\log \text{N V/C IV} \approx -0.25$. These ratios are compared to photoionization and collisional ionization models to constrain the excitation mechanism and the physical conditions of the line-emitting gas. We find that the collisional models do the poorest job of reproducing the data. The photoionization models reproduce the Si IV/C IV line ratios for some shapes of the ionizing spectrum, but the predicted N V/C IV line ratios are simultaneously too low by typically ~ 0.5 decades. Worse, for no parameters are any of the models able to reproduce the observed He II/C IV line ratios; this ratio is far too small in the collisional and scattering models and too large by typically ~ 0.5 decades in the photoionization models.

Subject headings: atomic processes — line: formation — stars: novae, cataclysmic variables — ultraviolet: stars

1. Introduction

During its 17 plus years of operation, the *International Ultraviolet Explorer* (*IUE*) satellite (Boggess et al. 1978) acquired a large number ($> 10^5$) of UV spectra from all classes of astronomical objects. Cataclysmic variables have been studied intensively with *IUE*, and these spectra have revealed a wide variety of phenomena which were previously unknown or poorly studied. These include mass loss via high-velocity winds, the heating and cooling of the white dwarf, the spectrum of the accretion disk, and the response of the disk to dwarf nova outbursts. As a result, we now have a much more complete understanding of the nature of CVs: the geometry, velocity law, mass-loss rate, and ionization structure of the wind; the disk instability mechanism and the heating and cooling waves which drive the disk to and from outburst; the relative energetics of the accretion disk and boundary layer; subclasses; and even evolutionary scenarios. These advances are due in part to the fact that CVs emit a large fraction of their luminosity in the UV.

With few exceptions, the strategy which has prevailed to date in the study of CVs with *IUE* and other instruments is to make an observation or set of observations of a single object and to analyze and interpret those data separately from the data of other similar objects. Only when this step is complete are the data compared with those from other similar objects. An alternative strategy is to examine the data from all the objects of a given class simultaneously. This is practical only in situations where a large body of data exists, of fairly uniform quality, and when the various members of a given class form a relatively homogeneous group. A few such studies of CVs using various manifestations of the *IUE* archive have appeared in the literature. Verbunt (1987) studied the absolute continuum spectral flux distributions of disk-fed CVs. la Dous (1991) studied the relative continuum spectral flux distributions of all classes of CVs, but concentrated on disk-fed systems. For the discrete spectral features, only the inclination dependence of the equivalent widths was discussed. Deng et al. (1994) studied the dependence on the orbital period and inclination of the relative continuum spectral flux distributions and the equivalent widths of the lines of dwarf novae in quiescence.

It is unfortunate that so little quantitative work has been performed to date on the emission lines of CVs. Emission lines are powerful diagnostics of the physical conditions in all types of objects including these interacting binaries. The emission line fluxes or relative fluxes can constrain the temperature, ionization state, density, elemental abundance, and geometrical distribution of the gas. However, the dependence of measurable quantities on these parameters is often complicated, necessitating numerical model fitting in many situations. The range of possible assumptions regarding the physical mechanisms of heating and ionization, together with the technical challenges of constructing models, add to the difficulty of performing such studies. As a result, emission lines have received less attention as diagnostics of CVs than have continuum properties.

In the present paper, we begin to remedy this situation with an analysis of the flux ratios of the emission lines of all classes of CVs using spectra extracted from the *IUE* Uniform Low

Dispersion Archive (ULDA). We begin by describing the data and our analysis procedures (§2). We then present the results of the data analysis (§3), followed by a discussion of models for the line emission (§4). In §5 we compare data and models and in §6 close with a summary of our conclusions.

2. Data Analysis

The *IUE* ULDA (Wamsteker et al. 1989) provides a unique source of archival data which satisfies the requirements for a comprehensive study of a large sample of objects owing to its uniform quality and the large number of spectra accumulated over the long life of *IUE*. Although the *IUE* final archive (Nichols-Bohlin et al. 1994) has since superseded the ULDA, the reprocessing effort of the final archive had not begun when this study was begun in 1992. To build the data sample, the *IUE* Merged Log was searched using software at the *IUE* Regional Analysis Facility, then at the University of Colorado. The search criteria were the camera (SWP), dispersion (low), and *IUE* object class (dwarf novae, classic novae, irregular variables, and nova-like variables). All spectra meeting these criteria were extracted from the ULDA resident at Goddard Space Flight Center, which at that time contained (nearly) all low-dispersion *IUE* spectra through 1988 (SWP sequence numbers through ≈ 35190). The spectra were then written to disk with header information extracted from the *IUE* Merged Log. Excluded from further consideration were 13 very early (prior to 1978 July) spectra of AM Her and SS Cyg lacking data quality flags. The final dataset consisted of ≈ 1300 spectra of ≈ 100 CVs.

From this dataset, we selected all spectra exhibiting pure emission lines. Sources which met this criteria include AM Her stars, DQ Her stars, dwarf novae in quiescence, and eclipsing nova-like variables and dwarf novae in outburst. To this dataset we added the *IUE* spectra of the eclipsing nova-like variable V374 Pup listed in Table 1 of Mauche et al. (1994), as we were working on that source at the time. Excluded from analysis were non-eclipsing nova-like variables and dwarf novae in outburst, since the UV resonance lines of such systems are either in absorption or are P Cygni profiles.

For these spectra, we measured the integrated fluxes above the continuum of the strongest emission lines in the SWP bandpass: N V $\lambda 1240$, Si IV $\lambda 1400$, C IV $\lambda 1550$, and He II $\lambda 1640$. To determine the flux of these lines, the continuum to the left and right of each line (e.g., from 1500–1530 Å and from 1570–1600 Å for C IV) was fitted with a linear function by the method of least squares. This method works well with all of the emission lines except N V, because the left side of this line falls on the wing of the geocoronal Lyman α emission line. To overcome this problem, a continuum point to the left of the N V line was specified interactively, and the fit included the region to the right of the line (1255–1270 Å) plus this continuum point to the left. Care was taken to insure that the continuum over this small wavelength region was a reasonable extrapolation both in normalization and slope to the continuum at longer wavelengths. In all cases the least-squares fit was made under the assumption that the errors σ_i in the flux density

f_i at each wavelength point λ_i were the same. After the normalization a and slope b of the continuum was determined, the size of the errors σ were estimated by assuming that the reduced χ^2 of the fit was equal to 1: $\sigma^2 = \sum_{i=1}^N (f_i - a - b\lambda_i)^2 / (N - 2)$. This procedure is necessary because the ULDA (unlike the *IUE* final archive) does not include the error associated with each flux point. The integrated fluxes of the emission lines were then determined by summing the flux minus the fitted continuum over the region of the line (e.g., 1530–1570 Å for C IV). The error on the integrated flux was determined by propagating the error σ through the calculation. Finally, careful track was kept of the number of pixels labeled by the data quality flags as either saturated or nearly saturated (extrapolated ITF). Such pixels compromise the quality of the flux density measurements and consequently the integrated line fluxes; saturated pixels are particularly bad in this regard, because they systematically produce only lower limits to the flux density. In the final cut to the data, flux measurements for a given line were retained only if the total number of saturated and extrapolated pixels included in the summation was less than or equal to some number n . While $n = 1$ would have been the ideal choice, such a stringent selection criterion would cull too many measurements. As a reasonable compromise, we settled on $n = 3$ for this selection criterion, allowing a few mild sinners to pass with the saints. The roster at this stage of the analysis consisted of ≈ 700 spectra of ≈ 60 CVs. Of this number, we present results based on ≈ 430 spectra of the 20 systems with the largest number (> 10) of flux measurements.

3. Observational Results

Just as color-color diagrams are a useful way to discuss the continuum spectral flux distributions of CVs (e.g., Wade 1988; Deng et al. 1994), flux ratio diagrams are a useful way to display and discuss the fluxes of their emission lines. Flux ratios remove the variables of luminosity and distance from the comparison of different sources; flux ratios are unaffected by aperture losses, which occur for *IUE* spectra obtained through the small aperture; and flux ratios are much less sensitive to reddening than the fluxes themselves. Due to the increase of the extinction efficiency at short wavelengths, reddening has the largest differential effect on the fluxes of the He II and N V lines. Luckily, for a typical extinction of $E_{B-V} \leq 0.1$ (Verbunt 1987), the ratio of the measured fluxes of these lines is only $\leq 18\%$ higher than intrinsic ratio. As we shall see, this correction, while systematic, is much smaller than either the typical measurement errors, or the typical dispersion in the flux ratios of any given source.

Of the many possibilities, we choose to plot the ratios N V $\lambda 1240$ /C IV $\lambda 1550$ and He II $\lambda 1640$ /C IV $\lambda 1550$ vs. Si IV $\lambda 1400$ /C IV $\lambda 1550$ (Figs. 1–8). In what follows, we often refer to these ratios simply as N V/C IV and He II/C IV vs. Si IV/C IV. It should be emphasized that the identifications of these lines are not unique; at $\Delta\lambda \approx 5$ Å, the *IUE* resolution is not sufficient to exclude several other possible lines in the vicinity of these wavelengths. We defer a discussion of such potential confusion, and of the physical motivation for our choice of lines until the following section, and begin by presenting the phenomenological behavior of these ratios as derived from

the data. We begin by discussing the various members of the various CV subclasses and then discuss the sources which do not appear to fit the pattern established by the other members of their subclass (sources we enjoy referring to as “weird”).

3.1. Results Arranged by Subclass

3.1.1. *AM Her stars: AM Her, V834 Cen, and QQ Vul*

Figure 1 shows that AM Her, V834 Cen, and QQ Vul form a sequence of increasing N V/C IV with increasing Si IV/C IV. He II/C IV is reasonable constant at $\approx 0.2 \pm 0.1$.

3.1.2. *DQ Her stars: EX Hya, TV Col, FO Aqr, and DQ Her*

Among these DQ Her stars, TV Col displays the greatest amount of variability in its continuum and line fluxes, and, as is evident in Figure 2, in its UV line ratios. The upper right portion of the observed range of line ratios is populated by the observations obtained during the optical and UV flare observed by Szkody & Mateo (1984); during the flare, both N V and He II increased relative to C IV. The relatively tight phase space occupied by the line ratios of FO Aqr is approximately the same as that of TV Col in outburst. The ionization state of the line-emitting gas in EX Hya and DQ Her is lower than the two other DQ Hers, as evidenced by their higher Si IV/C IV line ratios and the lower He II/C IV line ratios.

3.1.3. *Dwarf Novae in Quiescence: SS Cyg, SU UMa, RU Peg, and WX Hya*

As shown in Figure 3, WX Hya has the largest ratios of N V/C IV and Si IV/C IV among all the AM Her stars, DQ Her stars, and other dwarf novae in quiescence. SU UMa and RU Peg have N V/C IV ratios of ≈ 0.3 , but the value for SS Cyg is $\approx 30\%$ lower at ≈ 0.2 .

3.1.4. *Eclipsing Dwarf Novae: Z Cha and OY Car*

As shown in Figure 4, relative to all other “normal” CVs, Z Cha and OY Car both have strong N V relative to C IV. Almost all of the spectra of Z Cha were obtained during the peak and decline of the superoutburst of 1987 April (Harlaftis et al. 1992a) and of a normal outburst of 1988 January (Harlaftis et al. 1992b). The evolution of the spectrum during these observations is manifest most clearly in the Si IV/C IV ratio, which was highest during the decline of the superoutburst ($V \approx 12.3\text{--}12.7$) and lowest during the decline of the normal outburst ($V \approx 13.3\text{--}14.0$). During these intervals, both the N V/C IV and He II/C IV ratios remained

roughly constant, though there is some indication that the He II/C IV ratio increased as the Si IV/C IV ratio decreased. The spectra of OY Car were obtained during the decline of the superoutburst of 1985 May (Naylor et al. 1988) and produce flux ratios which roughly equal those of Z Cha in superoutburst.

3.1.5. *Eclipsing Nova-like Variables: UX UMa, V347 Pup, and RW Tri*

As shown in Figure 5, the eclipsing nova-like variables UX UMa, V347 Pup, and RW Tri have moderately strong N V relative to C IV, with N V/C IV ratios intermediate between those of dwarf novae in quiescence and eclipsing dwarf novae. The phase space occupied by V347 Pup is amazingly tight, and is disturbed only by eclipse effects: the single discrepant Si IV/C IV ratio was obtained from the eclipse spectrum of this source, and is due to that fact that the C IV emission line is eclipsed less than the other emission lines. The cause of the large spread in line ratios of UX UMa appears to be due to a different mechanism: there are epochs when Si IV is weak relative to C IV, and other epochs when it is reasonably strong. These epochs do not seem to correlate with the continuum flux. The He II/Si IV ratio of UX UMa is typically less than that of V347 Pup.

3.1.6. *Intercomparison of Various Subclasses*

Figure 6 combines the line ratios of the objects from the previous figures grouped together into magnetic (upper panels) and non-magnetic (lower panels) systems. It is apparent from this figure and the previous discussion that the line ratios of the various subclasses are rather homogeneous, with a dispersion of ~ 1 decade. This dispersion is due to almost equal contributions from the dispersion of values from the various observations of individual objects (~ 0.5 decade) and from the dispersion from one object to another (~ 0.5 decade).

There are clear and significant differences between these two subclasses: (i) He II/C IV is ~ 0.25 decades larger in magnetic systems; (ii) Si IV/C IV is slightly larger in the non-magnetic systems, but the difference is small compared to the dispersion; (iii) The upper limit on the N V/C IV distribution is greater in the non-magnetic systems, while the lower limit of the distribution is similar in the two cases.

It is also instructive to consider the differences within these two subclasses. The greater range of the N V/C IV distribution is due to the eclipsing dwarf novae Z Cha and OY Car (squares and circles, respectively, in the lower panels of Fig. 6); otherwise the N V/C IV distributions of magnetic and non-magnetic systems are similar. Among the magnetic systems, TV Col (triangles in the upper panels of Fig. 6) has significantly lower Si IV/C IV than any other object; the Si IV/C IV distribution would be much tighter if this object were excluded from the sample.

3.2. Systems Showing Anomalous Behavior: “Weird” CVs

3.2.1. *GK Per*

GK Per is unusual among CVs in a number of respects. It has an evolved secondary and hence a very long orbital period and a large accretion disk. Unlike most CVs, the UV continuum of this DQ Her-type system peaks in the *IUE* bandpass. The cause of this anomaly is thought to be due to the disruption of the inner disk by the magnetic field of the white dwarf (Bianchini & Sabadin 1983; Wu et al. 1989; Mauche et al. 1990; Kim et al. 1992). As shown in Figure 7, *GK Per* also distinguishes itself from other CVs in its anomalously large He II/C IV ratio. In outburst, both He II and N V are stronger than C IV, whereas the opposite is true in quiescence. While the Si IV/C IV ratio spans a rather broad range of ≈ 0.2 –1, this range is present in both outburst and quiescence.

3.2.2. *V Sge*

V Sge is an unusual nova-like variable which occasionally manifests brightenings of as much as 3 mag (Herbig et al. 1965). The model for this system is highly uncertain; both white dwarf and neutron star binary models have been considered (Koch et al. 1986; Williams et al. 1986). The *IUE* spectra of *V Sge* obtained during 1978 and 1979 are characterized by strong He II and N V emission lines relative to C IV (Koch et al. 1986): N V/C IV ≈ 2.5 and He II/C IV ≈ 3 . These distinguishing line ratios are suppressed in outburst. In 1985 August, the UV continuum was enhanced by factor of ≈ 2 relative to the earlier spectra, while the N V/C IV ratio fell to ≈ 0.4 and the He II/C IV ratio fell to ≈ 1 . In 1985 April, the UV continuum was enhanced by factor of ≈ 4 , while the N V/C IV ratio fell to ≈ 0.15 ; measurements of the He II/C IV ratio are not possible during this epoch because the He II emission line was overexposed. This behavior is opposite to that of *GK Per*, whose N V/C IV and He II/C IV ratios increased mildly in outburst.

3.2.3. *BY Cam*

BY Cam (H 0538+608) is one of only three AM Her stars above the period gap (*V1500 Cyg* and *AM Her* being the other two) and one of only two which rotates asynchronously (*V1500 Cyg* being the other one). As pointed out by Bonnet-Bidaud & Mouchet (1987), *BY Cam* is unusual in having weak C IV and strong N V. Figure 7 shows that all the line ratios are large because C IV is weak.

3.2.4. *AE Aqr*

AE Aqr exhibits a host of bizarre phenomena including variable flare-like radio and optical emission; rapid, coherent oscillations; and QPOs. Its UV spectrum has been discussed by Jameson et al. (1980) and is distinguished by the near-absence of C IV. Unfortunately, the flux measurements of the C IV emission line are very uncertain because this line is so weak and because the measurements are possibly contaminated by the Si II 3p–4s multiplet at 1526.71, 1533.43 Å (e.g., Kelley 1987). Nevertheless, it is clear that N V and Si IV have similar strengths and are ≈ 10 times stronger than He II and C IV, which have similar strengths.

4. Line Ratio Modeling

We now present some simple models for the systematic behavior we expect from CV line ratios. Although CVs as a class share a number of fundamental properties, they also differ between subclasses in the likely properties of the gas responsible for line emission. For example, in disk-fed systems, such as nova-like variables and dwarf novae, a possible site for line emission is the disk atmosphere. In this case, the atmosphere may be heated either by viscosity (e.g., Shaviv & Wehrse 1991) or by photons from other parts of the disk or from the vicinity of the white dwarf (e.g., Ko et al. 1996). A wind is also present in nova-like variables and dwarf novae in outburst (see Mauche & Raymond 1996 for a recent review of CV winds). In AM Her stars, the line emission may come from the stream of material being transferred from the secondary to the white dwarf which is heated either mechanically or by photons from the shock at the white dwarf surface. DQ Her stars may have emission from either or both of these sites.

Beyond these simple considerations, there is considerable uncertainty about the nature of the emission region: the geometrical arrangement of the gas relative to the source of ionizing photons (if present), the density and optical depth of the gas, the elemental abundances of the gas, the spectrum and flux of the ionizing radiation, and the presence and distribution of any other sources of heating. These quantities are not only uncertain, they may differ from one object to another in a subclass. Furthermore, all subclasses contain anomalous members. We therefore consider models for CV emission regions which employ the very simplest assumptions, namely, slab models each with a single ionizing spectrum, gas composition, and density. We then explore plausible choices for photon flux, column density, and mechanical heating rate (if any). The results serve not only as a test of the validity of the models when compared to the observations, but also provide insight into the physics of the line emission which will hopefully remain useful when more detailed models are considered.

Further support for this strategy comes from the results of the previous section: the objects of a given subclass show significant clustering in the two line ratio diagrams, and there are clear differences from one subclass to another. Therefore, we can define our modeling goals as follows: to test whether one or more sets of models can reproduce the mean values of the observed line

ratios for the various subclasses of objects, and to test whether any models can reproduce the dispersion or systematic variability of the observed line ratios. Given the uncertainties of the models and the observed dispersion in line ratios, we will consider agreement between the models and observations to be adequate if the two agree to within the dispersion of the observed values, i.e., approximately one decade. We will show that although this is clearly a very crude criterion, it turns out to be very constraining for the models.

4.1. Model Ingredients

Although the mechanism of line emission is uncertain, we favor photoionization as the source of ionization, excitation, and heating of the gas. This is partly because the observed continuum spectra, and their extrapolation into the unobservable spectral regions, provide a convenient and plausible energy source. Further support for this idea comes from Jameson et al. (1980) and King et al. (1983) who compared the observed line strengths from AE Aqr and UX UMa to simple predictions of both photoionized and coronal models and found the coronal models inconsistent with the observed lines. Nevertheless, for the sake of completeness, we examine both photoionized and coronal models.

The models are calculated using the XSTAR v1.19 photoionization code (Kallman & McCray 1982; Kallman & Krolik 1993). The models consist of a spherical shell of gas with a point source of continuum radiation at the center; this may be used to represent a slab in the limit that the shell thickness is small compared with the radius. In what follows we will use the line fluxes emergent from the illuminated face of the slab, which is equivalent to those emitted into the interior of the spherical shell. The input parameters include the source spectrum, the gas composition and density, the initial ionization parameter (determining the initial radius, see below for a definition), and the column density of the shell (determining the outer radius). Construction of a model consists of the simultaneous determination of the state of the gas and the radiation field as a function of distance from the source. The state of the gas at each radius follows from the assumption of a stationary local balance between heating and cooling and between ionization and recombination.

When the gas is optically thin, the radiation field at each radius is determined simply by geometrical dilution of the given source spectrum. Then, as shown by Tarter et al. (1969), the state of the gas depends only on the ionization parameter ξ , which is proportional to the ratio of the radiation flux to the gas density. We adopt the definition of the ionization parameter used by Tarter et al.: $\xi = L/(nr^2)$, where L is the ionizing energy luminosity of the central source (between 1 and 1000 Ry), n is the gas density, and r is the distance from the source. This scaling law allows the results of one model calculation to be applied to a wide variety of situations. For a given choice of spectral shape, this parameter is proportional to the various other customary ionization parameter definitions: $U_H = F_H/n$, where F_H is the incident photon number flux above the hydrogen Lyman limit; to $\Gamma = F_\nu(\nu_L)/(2hcn)$, where $F_\nu(\nu_L)$ is incident energy flux at the

Lyman limit; and to $\Xi = L/(4\pi R^2 cnkT)$. This simple picture breaks down when the cloud optical depth is non-negligible, since the source spectrum then depends on position, and the escape of cooling radiation in lines and recombination continua depends on the total column density of each ion species and hence on the ionization state of the gas throughout the cloud. In addition, the rates for cooling and line emission can depend on gas density owing to the density dependence of line collisional deexcitation and dielectronic recombination. However, even in this case the ionization parameter remains a convenient means of characterizing the results.

The state of the gas is defined by its temperature and by the ion abundances. All ions are predominantly in the ground state, and except for hydrogen and helium the populations of excited levels may be neglected. The relative abundances of the ions of a given element are found by solving the ionization equilibrium equations under the assumption of local balance, subject to the constraint of particle number conservation for each element. Ionization balance is affected by a variety of physical processes, most notably photoionization and radiative and dielectronic recombination. The temperature is found by solving the equation of thermal equilibrium, by equating the net heating of the gas due to absorption of incident radiation with cooling due to emission by the gas. These rates are derived from integrals over the absorbed and emitted radiation spectra. Although Compton scattering is not explicitly included as a source or sink of radiation, its effect is included in the calculation of the thermal balance.

The emitted spectrum includes continuum emission by bremsstrahlung and recombination and line emission by a variety of processes including recombination, collisions, and fluorescence following inner shell photoionization. Line transfer is treated using an escape probability formalism and includes the effects of line destruction by collisions and continuum absorption. Transfer of the continuum is calculated using a single stream approximation, as described in Kallman & McCray (1982).

Rates for atomic processes involving electron collisions have been modified since the publication of Kallman & McCray (1982) to be consistent with those used by Raymond & Smith (1977). Recombination and ionization rates for Fe have been updated to those of Arnaud & Raymond (1992). In addition, we have added many optical and UV lines from ions of medium-Z elements (C, N, O, Ne, Si, and S) using collisional and radiative rates from Mendoza (1983). The elements Mg, Ar, Ca, and Ni have also been added. The models have a total of 168 ions, producing 1715 lines, of which 665 have energies greater than 120 eV (10 Å), and approximately 800 are resonance lines. For each ion we also calculate the emission from radiative recombination onto all the excited levels which produce resonance lines. The number of such continua is equal to the number of resonance lines in the calculation. Some of the results of the models are sensitive to the rates for dielectronic recombination. We use the high temperature rates given by Aldrovandi & Pequignot (1973), together with the low temperature rates from Nussbaumer & Storey (1983). These rates differ significantly for several relevant ions, e.g., Si III, relative to those of Shull & Van Steenberg (1983), which were used in most earlier versions of XSTAR. Finally, all models assume element abundances which are close to solar: H:He:C:N:O:Ne:Mg:Si:S:Ar:Ca:Fe:Ni =

1:0.1:3.7E-4:1.1E-4:6.8E-4:2.8E-5:3.5E-5:3.5E-5:1.6E-5:4.5E-06:2.1E-6:2.5E-5:2.0E-6 (Withbroe 1971).

An emission line may be produced by two types of physical processes. First is what we will call “thermal emission,” which is recombination or collisional excitation by thermal electrons. Second is excitation by photons from the incident continuum. Since this is an elastic scattering process, we will refer to it as “scattering.” This process will produce an apparent emission feature if our line of sight to the continuum source is at least partially blocked, and the scattering region must be concentrated on the plane of the sky (see Krolik & Kriss 1995 for more discussion of these issues). If the scattering region has a bulk velocity greater than the thermal line width then a P Cygni or inverse P Cygni profile will form even if the scattering region is spherical. Scattering fails to account for the presence of He II λ 1640, since this is a subordinate line and the population of the lower level will be negligibly small under conditions appropriate to photoionized gas. Significant opacity in this line would require a temperature greater than $\sim 3 \times 10^5$ K and level populations which are close to LTE values. In spite of this, we have investigated the possibility that this mechanism can explain the ratios of the other lines we consider. We assume that the fluxes in scattered lines are proportional to the opacities in the lines. This is likely to be justified if the line optical depths are less than unity, and if the wind ionization balance is approximately uniform. If so, the line flux ratios will equal the opacity ratios.

4.2. Input Parameters

The models we explore fall into two categories: photoionized models and collisional (coronal) models. For each we present the line ratios for both thermal emission and scattering emission mechanisms. The photoionization model parameters are chosen in an attempt to crudely represent the range of observed ionizing spectra from CVs. These typically consist of a soft component which is consistent with a 10–50 eV blackbody, together with a hard X-ray component such as a 10 keV bremsstrahlung (e.g., Córdova & Mason 1982a). The ratio of strengths of these two components varies from one object to another, and with outburst state and subclass. However, a typical ratio is 100:1 (soft:hard) for non-magnetic systems, and 1:1 for magnetic systems (Córdova & Mason 1982b). Beyond such simple considerations, the detailed shape of the ionizing radiation field is difficult to determine accurately. This is due to the strong influence of photoelectric absorption by interstellar and circumstellar gas, and to the limited bandpass and spectral resolution of most past observations in the soft X-ray band (e.g., Ramsay et al. 1994; Mauche 1996). Owing to such uncertainties we choose a few very simple ionizing spectra for consideration in our photoionization models: Model A: 30 eV blackbody, Model B: 10 keV brems, Model C: 50 eV blackbody, Model D: 10 eV blackbody. Model G is the mechanically heated (coronal) ionization model. All these models have a total (neutral + ionized) hydrogen column density of $N_{\text{H}} = 10^{19} \text{ cm}^{-2}$, chosen to make them optically thin to the continuum and effectively thin to the escaping resonance lines. In addition, we present two photoionized models which are close to being optically thick, both

of which have of column density $N_{\text{H}} = 10^{23} \text{ cm}^{-2}$. Model E has a 30 eV blackbody ionizing spectrum, and Model F has a 10 keV brems ionizing spectrum. For each model we determine the net line flux contained in the wavelength intervals 1237–1243 Å, 1390–1403 Å, 1547–1551 Å, and 1639–1641 Å, which we refer to as N V, Si IV, C IV, and He II, respectively. As we will show, these wavelength intervals also contain other lines which can mimic these strong lines, and these other lines are likely to affect the interpretation of the *IUE* low resolution data as well. The results of our models—the Si IV/C IV, N V/C IV, and He II/C IV line ratios—are summarized in Tables 1–3. For the photoionization models, we consider various values of the ionization parameter for six choices of ionizing continuum shape. For the collisional models, we consider ten values of the gas temperature. We also tested for the dependence on gas density and found that it is negligible for the conditions we consider; all the models presented here have density $n = 10^9 \text{ cm}^{-3}$.

4.3. Model Results

When the line ratios shown in Tables 1–3 are plotted in two diagrams in the same way as the *IUE* data, several common properties emerge. These are shown in Figures 9 and 10, with various symbols denoting the ionizing spectra: Model A ■, Model B = ●, Model C = ×, Model D = +, Model E = □, Model F = ○. We have also tried a model consisting of a 30 eV blackbody together with a 10 keV brems spectrum in a ratio of 99:1; the results are so similar to Model A as to be indistinguishable, i.e., the 30 eV blackbody has far more influence on the ionization balance than does the 10 keV brems in these ratios. Model G, the coronal case, produces line ratio combinations which are almost entirely outside the range spanned by these figures. For the other spectra, as expected, there is little or no dependence on model density for optically thin photoionized models.

The shape of the trajectory of the model results in these planes is similar for most of the models. They resemble a U shape, although in some cases the right upright of the U is missing, and in others it is tipped nearly 45 degrees to the vertical. We can understand the results better if we label the points along the U as follows: A = upper left extreme of trajectory; B = bottom of steepest part of left upright; C = lowest point of trajectory; D = bottom of right upright; E = upper right extreme of trajectory. These are shown schematically in Figure 11. In general, the trajectory is traversed from point A to point E as the ionization parameter decreases, and may be understood in terms of the relative ease of ionization of the various ions responsible for line emission. The ionization parameter at which the abundance of a given ion peaks, relative to its parent element, can be derived crudely from the ionization potential. Thus, the four ions responsible for the strongest observed lines may be ordered in terms of decreasing ease of ionization according to: Si IV, He II, C IV, N V. For the metal ions the ionization parameter at which the emissivities of the lines peak is approximately the same as the ionization parameter at which the ion abundances peak. Thus, at the highest ionization parameters we consider, nitrogen is ionized to or beyond N V, carbon is ionized beyond C IV, and silicon is ionized beyond Si IV. However, the abundance of N V, and hence its line emissivity, is greater than the corresponding

quantities for C IV, which in turn are greater than for Si IV. Thus, at high ionization parameter, N V/C IV is relatively large and Si IV/C IV is small, corresponding to point A of the trajectory in the N V/C IV vs. Si IV/C IV plane. At intermediate ionization parameter, carbon recombines to C IV and nitrogen recombines below N V, so that N V/C IV is small and Si IV/C IV is also small (point B). At lower ionization parameter, silicon recombines to Si IV and carbon may recombine to below C IV, resulting in an intermediate value of Si IV/C IV (point C). At very low ionization parameter, Si IV/C IV is at a maximum, and there is an apparent increase in N V/C IV (points D, E). This cannot be understood in terms of conventional ionization balance, since the C IV abundance always exceeds the N V abundance at low ionization parameter. Rather, it is due to confusion between the N V 2s–2p doublet at 1238.82, 1242.80 Å and the Mg II 3s–4p doublet at 1239.93, 1240.39 Å (e.g., Kelley 1987). Since Mg II has a lower ionization potential than any of the other ions in question, Mg II/C IV increases at low ionization parameter, thus explaining the apparent increase in N V/C IV.

The behavior of He II λ 1640 differs from the other lines owing to the fact that it is emitted by recombination, while the others are emitted by collisional excitation. Thus, the emissivity of He II λ 1640 remains nearly constant at high ionization parameter, while the C IV λ 1550 line emissivity decreases with increasing ionization parameter. This is in spite of the fact that He II is more easily ionized than C IV. This explains the AB part of the trajectory in the He II/C IV vs. Si IV/C IV plane. As the ionization parameter decreases, C IV recombines to C III and below, while He II and He III are still abundant, thus explaining the DE part of the trajectory.

The model behavior under the scattering scenario is qualitatively similar to the thermal excitation scenario, except for the weakness of He II. The line strengths in the scattering case are less dependent on the gas temperature than in the thermal excitation case, and the oscillator strength for the Mg II 3s–4p transition is small, so that the trajectory lacks the DE segment in the N V/C IV vs. Si IV/C IV plane.

The fact that the coronal models fail almost completely to produce line ratios within the range of our diagrams indicates that it is unlikely that this process dominates in CV line-emitting gas. This result is not surprising, owing to the well-known fact that coronal equilibrium produces ion abundances that have less overlap in parameter space (e.g., temperature) between adjacent ion stages than does photoionization.

4.4. Spectral Dependence

The shape of the ionizing spectrum influences the location of the various points along the trajectory in the two line ratio diagrams, and also the existence of part of the trajectory, most notably the segments between points C and E.

For soft spectra, such as the 30 eV blackbody, recombination to species below Si IV does not occur for the parameter range considered ($\log \xi = -1.5$ to $+1.0$), so the CDE part of the trajectory

is absent in the N V/C IV vs. Si IV/C IV plane. Also, when the ionization parameter is suitable for producing large N V/C IV, the Si IV/C IV ratio is so small as to be off the scale of Figure 9.

For very soft spectra, such as the 10 eV blackbody, there are insufficient hard photons to produce N V. Thus, points A and B are missing in the N V/C IV vs. Si IV/C IV plane. The DE part of the trajectory is entirely due to Mg II λ 1240.

For hard spectra, such as the 10 keV brems spectrum, X-rays can make Si IV via Auger ionization even at very low ionization parameter. Thus, the range of Si IV/C IV is greatly expanded, and can reach 10 at point D in the N V/C IV vs. Si IV/C IV plane. Other models, such as a 30 eV blackbody, can make large Si IV/C IV at low ionization parameter, but they also have very weak N V line emission, so that the 1240 Å feature is dominated by Mg II and they are on DE segment of the trajectory.

At high ionization parameter He II is a “bolometer” of the ionizing spectrum, since it is dominated by recombination. That is, the He II strength depends only on the number of photons in the He II Lyman continuum ($\varepsilon \geq 54.4$ eV). So, harder spectra make stronger He II, and conversely. This behavior may still hold at point C. At small ionization parameter, He II is likely to be more abundant than C IV or Si IV. This explains the CDE segment of the trajectory in the He II/C IV vs. Si IV/C IV plane. This fact does not seem to depend strongly on spectral shape, although the value of Si IV/C IV at points C, D, and E does depend on the spectrum; this ratio increases at all these points for harder spectra, and conversely.

The 10 eV blackbody models show a “hook” in their trajectory in which the Si IV/C IV appears to increase with increasing ionization parameter at the upper end of the range of values we consider. This is counter to the expected behavior of Si IV at high ionization parameter, since we expect silicon to become ionized beyond Si IV and the Si IV abundance to decrease at high ionization parameter. The reason for the model behavior is the confusion between the Si IV doublet at 1393.76, 1402.77 Å and the O IV $2s^2 2p-2s2p^2$ multiplet at 1397–1407 Å (e.g., Kelley 1987). The unique behavior of the 10 eV blackbody models is due to the fact that the O IV lines increase at high ionization parameter only for the softest spectra; harder spectra ionize oxygen past O IV when other ion abundances are at similar values. Like the N V and Mg II lines near 1240 Å, the Si IV and O IV lines near 1400 Å can be confused in *IUE* low resolution data.

The overlap in ionization parameter space of the regions where N V, Si IV, C IV, and He II predominate does not differ greatly between models with hard X-ray spectra (e.g., 10 keV brems) and those with blackbodies with $kT > 30$ eV. A more pronounced difference is due to the fact that the latter spectra have all their ionizing photons crammed into a smaller energy range. Therefore, the ionization parameter scale, which simply counts the energy in ionizing photons, and the distribution of ionization, which really depends on the photon density in the EUV/soft X-ray region, are very different in the two cases. For example, in the 10 keV brems case, C IV predominates at $\log \xi = 0$, while in the 30 eV blackbody case it predominates near $\log \xi = -1$. Thus, our model grid, which spans the range $-3 < \log \xi < +1.5$, does not include the region where

the gas has recombined below C IV, etc., in the blackbody case. This accounts for the absence of the CDE part of the line ratio trajectory for the blackbody models.

5. Comparison with Observations

The models presented in the previous section provide a useful context in which to examine the likely physical conditions in CV line-emitting regions. As was discussed earlier, we do not expect these simple models to account for the details of the observed spectra, but we do hope that they will at least crudely reproduce some of the features of the observations. These might include: the range of the observed ratios to within the dispersion of the observed values, i.e., approximately one decade, and possibly the differential behavior of a given source as it varies in time. In fact, we find little evidence for agreement between the observations and any of the models beyond the simplest measures of consistency for some of the line ratios. We begin the comparison of model results with observations by considering the “normal” CVs.

5.1. “Normal” CVs

The observed ratios of “normal” CVs lumped together regardless of class (Fig. 6) are clustered within a range of ~ 1 decade for $\log \text{Si IV/C IV} \approx -0.5$ and $\log \text{He II/C IV} \approx -1.0$ and ~ 1.5 decades for $\log \text{N V/C IV} \approx -0.25$. The larger range of the N V/C IV ratio is due largely to the large line ratios of the eclipsing dwarf novae Z Cha and OY Car (squares and circles, respectively, in Fig. 6). Otherwise, the range is ~ 1 decade centered on ≈ -0.5 . This same general range is spanned by the models, but there is little detailed agreement.

One notable failure of the models is the behavior in the He II/C IV vs. Si IV/C IV plane. The photoionization models always produce $\text{He II/C IV} \gtrsim \text{Si IV/C IV}$. This is because, although the He II line is emitted following radiative recombination and the C IV and Si IV lines are formed by collisional excitation, photons at energies greater than 54.4 eV which are responsible for ionizing He II are also responsible for heating the gas. So, models which efficiently heat the gas and emit Si IV and C IV also have efficient ionization of He II and hence efficient production of the 1640 Å line. In contrast, “normal” CVs show He II/C IV values which are less than Si IV/C IV by ~ 0.5 decades. Magnetic systems have He II/C IV line ratios which are systematically higher (and Si IV/C IV line ratios which are systematically lower) than those of the non-magnetic systems by ~ 0.25 decades. Only the DQ Her stars TV Col and FO Aqr (triangles and pentagons, respectively, in Fig. 6) have $\text{He II/C IV} \geq \text{Si IV/C IV}$.

It is interesting to note that the “hook” in the trajectory of the 10 eV blackbody models referred to in the previous section occurs near the values of these line ratios where most observed objects cluster. Furthermore, the 10 eV models come closest to reproducing the observed He II/C IV ratios; they are the only ones for which He II/C IV falls below Si IV/C IV.

The coronal models produce He II/C IV values of order 1% of Si IV/C IV when this latter ratio is in the observed range; even at this relatively favorable point, the N V/C IV ratio is much smaller than observed. This suggests that the coronal emission mechanism is less likely than photoionization for all CVs.

In the N V/C IV vs. Si IV/C IV plane, the models and the data span a similar range of ratios, so there is less indication of the failure of any of the models. The 50 eV blackbody models are least successful at reproducing the most commonly observed values of these ratios simultaneously. The 30 eV blackbody and 10 keV brems models both span the observed range, as do the optically thick models (which also use these ionizing spectra). The “hook” in the trajectory of the 10 eV blackbody models causes the Si IV/C IV ratio to lie almost entirely in the range $-1.5 \leq \log \text{Si IV/C IV} \leq -0.5$, which is close to that spanned by the observed ratios of most “normal” CVs.

In addition to asking whether there exists a model which can reproduce a given ratio, we can ask whether the distribution of observed ratios is consistent with the analogous model quantity. For example, if the ionizing spectrum and emission mechanism are independent of time, but the luminosity and hence the ionization parameter varies with time, we expect that the ratios of a given object will lie along a U-shaped trajectory in the line ratio diagram. In contrast, there appears no clear pattern in the observed ratios for objects with many observations, other than a clustering in a well-defined region of the diagram.

5.2. “Weird” CVs

Consider next the “weird” CVs. Figures 7 and 8 demonstrate that V Sge, GK Per, BY Cam, and AE Aqr form a sequence of dramatically increasing Si IV/C IV and N V/C IV at nearly constant He II/C IV. In V Sge and GK Per, He II/C IV > Si IV/C IV, unlike most of the “normal” CVs, but consistent with the photoionization models. The extreme line ratios of BY Cam and AE Aqr are harder to understand. Bonnet-Bidaud & Mouchet (1987) have suggested a depletion of carbon by a factor of ~ 10 to explain the anomalous line ratios of BY Cam. If a similar deficiency applies to AE Aqr, depletion by a factor of ~ 60 is required. Although such abundance anomalies are possible, they are unlikely to explain the positive correlation between N V/C IV and Si IV/C IV observed in AE Aqr and possibly BY Cam (see Figs. 7 and 8). The observed correlation between these ratios lends support to the hypothesis that confusion between the N V 2s–2p doublet and the Mg II 3s–4p doublet, together with a low value of the ionization parameter and hence a large value of the Si IV/C IV ratio, is responsible for the apparent anomalous line ratios of BY Cam and AE Aqr. However, none of the models reproduce the nearly perfect linear proportionality between N V/C IV and Si IV/C IV observed in AE Aqr.

There are several possibilities why the models and the observed line ratios are discrepant. First, it is possible that we have failed to consider ionizing spectra of the right type. Since the 10 eV blackbody appears to come closest to providing agreement with the He II/C IV and

Si IV/C IV ratios simultaneously, it is possible that there are confusing lines which we have not included in our models, or which become important under other conditions, which affect the results. Alternatively, the emission region may consist of multiple components with differing physical conditions. If so, the various components must have line ratios which bracket the observed values. This is ruled out by our models: no single set of models brackets the observed ratio of He II/C IV, for example. The observed values of this ratio are bracketed by the photoionization models on the high side and the coronal models on the low side, so that a superposition of these models might provide consistent line ratios. However, we consider this possibility to be somewhat contrived, and a more detailed exploration is needed to test whether it can account for all the ratios simultaneously. Another possible explanation for the He II/C IV ratio is that our assumption of a stationary steady state is invalid for the line-emitting region. If, for example, the heating and ionization of the gas occurs as the result of many impulsive events, then the time-average value of the ratios could differ significantly from the steady-state model predictions owing to the differing timescales for relaxation of the upper levels of the He II line from that of C IV. Such a scenario has been suggested to account for the strength of the He II lines from the Sun (Raymond 1990). The differential behavior of the line ratios from a given object could be due at least in part to changes in the ionizing spectrum or ionization mechanism, rather than simply due to changes solely in ionization parameter. This could account for the departures from the variability behavior predicted by the models. In spite of the difficulty in reproducing the observed line ratios, steady-state photoionization models are capable of fitting the absolute strengths of the observed lines (Ko et al. 1996).

6. Summary

We have presented a statistical analysis of the Si IV/C IV, N V/C IV, and He II/C IV emission line ratios of 20 CVs based on ≈ 430 UV spectra extracted from the *IUE* ULDA. We find for most systems that these ratios are clustered within a range of ~ 1 decade for $\log \text{Si IV/C IV} \approx -0.5$ and $\log \text{He II/C IV} \approx -1.0$ and ~ 1.5 decades for $\log \text{N V/C IV} \approx -0.25$. The larger range of the N V/C IV ratio is due largely to the large line ratios of the eclipsing dwarf novae Z Cha and OY Car; otherwise, the range of $\log \text{N V/C IV}$ is ~ 1 decade centered on ≈ -0.5 . The clearest difference between magnetic and non-magnetic CVs is the He II/C IV ratio, which is ~ 0.25 decades larger in magnetic systems.

To place constraints on the excitation mechanism and the physical conditions of the line-emitting gas of CVs, we have investigated the theoretical line ratios of gas in either photoionization and collisional ionization equilibrium. Given the uncertain and variable geometry, density, optical depth of the line-emitting gas and the shape and luminosity of the ionizing spectrum, we have restricted ourselves to consideration of simple slab models each with fixed gas composition, density, and column density. The variables have been the shape and ionization parameter of the ionizing spectrum and the density and column density of the slab; for the collisional models, the

temperature was varied. Line emission is produced in these models by recombination or collisional excitation by thermal electrons or by excitation by the ionizing continuum (“scattering”).

Within the confines of these simple models, we find little agreement between the observations and any of the models. Specifically, the observed Si IV/C IV line ratios are reproduced by many of the models, but the predicted N V/C IV line ratios are simultaneously too low by typically ~ 0.5 decades. Worse, for no parameters are any of the models able to reproduce the observed He II/C IV line ratios; this ratio is far too small in the collisional and scattering models and too large by typically ~ 0.5 decades in the photoionization models. Among the latter, the 10 eV blackbody models do the best job of reproducing the three line ratios simultaneously, but the match with the N V/C IV line ratio is accomplished only if the observed emission feature near 1240 Å is due to the Mg II 3s–4p doublet at 1239.93, 1240.39 Å instead of the N V 2s–2p doublet at 1238.82, 1242.80 Å.

Despite the above generally unfavorable comparisons between observations and simple photoionization and collisional models, our investigation has proven useful in revealing both the problems and promises of understanding the UV line ratios of CVs. Future detailed work could be profitably performed on any and all of the above CV subclasses with more detail in the shape of the ionizing spectrum and the geometrical distribution, density, and column density of the emission region(s). Where the distance is well known, not only line ratios but absolute line strengths can be fit. With larger effective area, weaker lines, less subject to optical depth effects, can be included. With higher spectral resolution, the UV lines be can uniquely identified, thus removing the annoying ambiguity of some of the line identifications. Additional constraints on the physical conditions and optical depth of the line-emitting gas is possible if the UV doublets are resolved. At comparable or slightly higher spectral higher resolution, the velocity field of the line-emitting gas can be constrained to constrain the ionization parameter and hence the density. With realistic photon transport in the models, the line shapes further constrain the models. By extending the bandpass into the far-UV, lines from species with both lower and higher ionization potentials (e.g., C III, N III, O VI, P V, S IV, S VI) provide additional diagnostics. The UV data can and is being obtained with *HST*, but to obtain the far-UV data, we require the likes of *HUT* (e.g., Long 1996), *ORFEUS* (e.g., Raymond et al. 1995), and *FUSE*.

We thank John Raymond for useful insights and suggestions and the referee for helpful comments which significantly improved the original manuscript. Work at Lawrence Livermore National Laboratory was performed under the auspices of the U.S. Department of Energy under contract No. W-7405-Eng-48.

TABLE 1
PHOTOIONIZATION MODEL LINE RATIOS

$\log \xi$	$\log \text{Si IV/C IV}$	$\log \text{N V/C IV}$	$\log \text{He II/C IV}$
Model A: 30 eV Blackbody Spectrum: ■			
–1.5	0.00	–2.02	0.68
–1.0	–0.55	–1.40	–0.44
–0.5	–1.12	–0.97	–0.90
0.0	–1.56	–0.59	–0.76
0.5	–2.20	–0.37	–0.58
1.0	–2.92	–0.24	–0.41
Model B: 10 keV Bremsstrahlung Spectrum: ●			
–1.5	0.78	0.91	3.65
–1.0	0.73	–0.15	2.99
–0.5	0.62	–1.38	1.87
0.0	0.19	–1.39	0.52
0.5	–0.76	–1.15	–0.64
1.0	–1.05	–0.68	–0.84
Model C: 50 eV Blackbody Spectrum: ×			
–3.0	1.54	2.18	5.06
–2.5	1.26	1.04	4.19
–2.0	0.97	–0.25	3.16
–1.5	0.67	–1.66	1.90
–1.0	0.11	–1.69	0.47
–0.5	–1.00	–1.17	–0.71
0.0	–2.01	–0.97	–0.90
0.5	–2.69	–0.62	–0.67
1.0	–3.20	–0.26	–0.32
1.5	–3.56	0.22	0.31

TABLE 1 — continued
PHOTOIONIZATION MODEL LINE RATIOS

$\log \xi$	$\log \text{Si IV/C IV}$	$\log \text{N V/C IV}$	$\log \text{He II/C IV}$
Model D: 10 eV Blackbody Spectrum: +			
–3.0	–1.86	0.35	3.50
–2.5	–1.50	–0.90	2.30
–2.0	–0.86	–2.23	1.06
–1.5	–0.48	–2.90	0.15
–1.0	–0.71	–2.52	–0.48
–0.5	–0.90	–1.88	–0.75
0.0	–0.80	–1.08	–0.79
0.5	–0.58	–0.31	–0.69
1.0	–0.45	0.25	–0.48
1.5	–0.45	0.57	–0.16
Model E: 30 eV Blackbody Spectrum, $\log N_{\text{H}} = 23$: \square			
–1.5	0.15	–1.83	1.46
–1.0	–0.31	–1.47	0.18
–0.5	–0.74	–1.13	–0.49
0.0	–0.90	–0.96	–0.59
0.5	–0.93	–0.92	–0.58
1.0	–0.93	–0.91	–0.58
1.5	–0.93	–0.89	–0.58
Model F: 10 keV Bremsstrahlung Spectrum, $\log N_{\text{H}} = 23$: \circ			
–1.5	0.86	1.33	4.20
–1.0	0.77	0.44	3.49
–0.5	0.67	–0.81	2.42
0.0	0.30	–1.36	1.05
0.5	–0.37	–1.15	–0.07
1.0	–0.69	–0.91	–0.44
1.5	–0.73	–0.79	–0.48

TABLE 2
SCATTERING MODEL LINE RATIOS

$\log \xi$	$\log \text{Si IV/C IV}$	$\log \text{N V/C IV}$	$\log \text{He II/C IV}$
Model A': 30 eV Blackbody Spectrum: ■			
-1.5	0.36	-1.44	-9.44
-1.0	-0.26	-0.98	-8.84
-0.5	-1.06	-0.65	-8.04
0.0	-1.86	-0.33	-6.40
0.5	-3.09	-0.19	-4.86
1.0	-4.65	-0.13	-3.35
1.5	-6.36	-0.10	-2.23
Model B': 10 keV Bremsstrahlung Spectrum: ●			
-1.5	1.26	0.68	-12.02
-1.0	1.20	0.08	-10.71
-0.5	1.07	-0.71	-9.49
0.0	0.68	-0.86	-8.10
0.5	-0.59	-0.81	-7.14
1.0	-2.25	-0.47	-4.57
1.5	-5.26	-0.06	-0.79
Model C': 50 eV Blackbody Spectrum: ×			
-3.0	2.01	1.86	-11.36
-2.5	1.70	1.02	-10.81
-2.0	1.41	0.07	-10.32
-1.5	1.10	-0.97	-9.69
-1.0	0.53	-1.24	-8.85
-0.5	-0.75	-0.79	-8.45
0.0	-2.23	-0.68	-7.13
0.5	-4.35	-0.42	-5.09
1.0	-6.98	-0.14	-3.19
1.5	$-\infty$	0.26	-1.42

TABLE 2 — continued
SCATTERING MODEL LINE RATIOS

$\log \xi$	$\log \text{Si IV/C IV}$	$\log \text{N V/C IV}$	$\log \text{He II/C IV}$
Model D': 10 eV Blackbody Spectrum: +			
–3.0	–1.28	0.35	–11.04
–2.5	–1.24	–0.48	–10.32
–2.0	–0.61	–1.41	–9.50
–1.5	–0.13	–2.22	–9.62
–1.0	–0.45	–2.06	–9.77
–0.5	–0.85	–1.48	–9.57
0.0	–1.08	–0.74	–8.62
0.5	–1.16	–0.02	–7.52
1.0	–1.19	0.51	–6.85
1.5	–1.20	0.81	–6.52
Model E': 30 eV Blackbody Spectrum, $\log N_{\text{H}} = 23$: \square			
–1.5	2.01	0.92	–6.19
–1.0	1.85	0.27	–5.06
–0.5	1.85	–0.03	–3.90
0.0	1.90	–0.01	–2.24
0.5	1.90	–0.02	–0.77
1.0	1.92	–0.18	0.58
1.5	1.96	0.09	1.91
Model F': 10 keV Bremsstrahlung Spectrum, $\log N_{\text{H}} = 23$: \circ			
–1.5	1.23	1.21	–11.89
–1.0	1.19	0.77	–10.29
–0.5	1.19	0.28	–8.47
0.0	1.19	–0.21	–6.36
0.5	1.14	–0.62	–4.50
1.0	1.08	–0.79	–1.93
1.5	1.05	–0.81	1.19

TABLE 3
COLLISIONAL IONIZATION MODEL LINE RATIOS

T (10,000 K)	$\log \text{Si IV/C IV}$	$\log \text{N V/C IV}$	$\log \text{He II/C IV}$
Model G: Constant Temperature			
3	-0.12	-2.63	-1.67
5	-0.46	-3.00	-2.61
7	-1.83	-2.91	-3.54
9	-2.65	-2.79	-4.04
11	-2.80	-2.16	-3.99
13	-2.65	-1.29	-3.58
15	-2.44	-0.52	-3.13
17	-2.29	0.04	-2.74
19	-2.17	0.38	-2.42
21	-2.09	0.52	-2.16

REFERENCES

- Aldrovandi, S., & Pequignot, D. 1973, *A&A*, 25, 137; 1976, 47, 321
- Arnaud, M., & Raymond, J. 1992, *ApJ*, 398, 394
- Bianchini, A., & Sabadin, F. 1983, *A&A*, 125, 112
- Boggess, A., et al. 1978, *Nature*, 275, 372
- Bonnet-Bidaud, J. M., & Mouchet, M. 1987, *A&A*, 188, 89
- Córdova, F. A., & Mason, K. O. 1982a, in *Accretion Driven Stellar X-ray Sources*, ed. W. H. G. Lewin & E. P. J. van den Heuvel (Cambridge: CUP), 147
- Córdova, F. A., & Mason, K. O. 1982b, *ApJ*, 260, 716
- Deng, S.-B., Zhang, Z.-Y., & Chen, J.-S. 1994, *A&A*, 281, 759
- Harlaftis, E. T., Hassall, B. J. M., Naylor, T., Charles, P. A., & Sonneborn, G. 1992a, *MNRAS*, 257, 607
- Harlaftis, E. T., Naylor, T., Hassall, B. J. M., Charles, P. A., Sonneborn, G., & Bailey, J. 1992b, *MNRAS*, 259, 593
- Herbig, G. H., Preston, G. W., Smak, J., Paczyński, B. 1965, *ApJ*, 141, 617
- Jameson, R. F., King, A. R., & Sherrington, M. R. 1980, *MNRAS*, 191, 559
- Kallman, T. R., & Krolik, J. H. 1993, NASA Internal Report
- Kallman, T. R., & McCray, R. 1982, *ApJS*, 50, 263
- Kelley, R. L. 1987, *Atomic and Ionic Spectrum Lines below 2000 Angstroms: Hydrogen through Krypton* (New York: AIP)
- Kim, S.-W., Wheeler, J. C., & Mineshige, S. 1992, *ApJ*, 384, 269
- King, A. R., Frank, J., Jameson, R. F., & Sherrington, M. R. 1983, *MNRAS*, 203, 677
- Ko, Y.-K., Lee, Y. P., Schlegel, E. M., & Kallman, T. R. 1996, *ApJ*, 457, 363
- Koch, R. H., Corcoran, M. F., Holenstein, B. D., & McCluskey, G. E. 1986, *ApJ*, 306, 618
- Krolik, J. H., & Kriss, G. A. 1995, *ApJ*, 447, 512
- la Dous, C. 1991, *A&A*, 252, 100
- Long, K. S. 1996, in *Cataclysmic Variables and Related Objects*, ed. A. Evans and J. H. Wood (Dordrecht: Kluwer), in press

- Mauche, C. W. 1996, in *X-ray Imaging and Spectroscopy of Cosmic Hot Plasmas*, ed. F. Makino (Tokyo: Universal Academy Press), in press
- Mauche, C. W., Miller, G. S., Raymond, J. C., & Lamb, F. K. 1990, in *Accretion-Powered Compact Binaries*, ed. C. W. Mauche (Cambridge: CUP), 195
- Mauche, C. W., & Raymond, J. C. 1996, in *Cosmic Winds and the Heliosphere*, ed. J. R. Jokipii, C. P. Sonett, & M. S. Giampapa (Tucson: Univ. of Arizona Press), in press
- Mauche, C. W., Raymond, J. C., Buckley, D. A. H., Mouchet, M., Bonnell, J., Sullivan, D. J., Bonnet-Bidaud, J.-M., & Bunk, W. H. 1994, *ApJ*, 424, 347
- Mendoza, C. 1983, in *IAU Symposium 103, Planetary Nebulae*, ed. D. R. Flower (Dordrecht: Reidel), 143
- Naylor, T., Bath, G. T., Charles, P. A., Hassall, B. J. M., Sonneborn, G., van der Woerd, H., & van Paradijs, J. 1988, *MNRAS*, 231, 237
- Nichols-Bohlin, J., Garhart, M., De La Peña, M., & Bushouse, H. 1994, *IUE NASA Newsletter*, No. 53
- Nussbaumer, H., & Storey, P. J. 1983, *A&A*, 126, 75
- Ramsay, G., Mason, K. O., Cropper, M., Watson, M. G., & Clayton, K. L. 1994, *MNRAS*, 270, 692
- Raymond, J. C. 1990, *ApJ*, 367, 387
- Raymond, J. C., Mauche, C. W., Bowyer, S., & Hurwitz, M. 1995, *ApJ*, 440, 331
- Raymond, J. C. & Smith, B. W. 1977, *ApJS*, 35, 419
- Shaviv, G., & Wehrse, R. 1991, *A&A*, 251, 117
- Shull, J. M., & Van Steenberg, M. 1983, *ApJS*, 48, 95
- Szkody, P., & Mateo, M. 1984, *ApJ*, 280, 729
- Tarter, C. B., Tucker, W., & Salpeter, E. E. 1969, *ApJ*, 156, 943
- Verbunt, F. 1987, *A&AS*, 71, 339
- Wade, R. A. 1988, *ApJ*, 335, 394
- Wamsteker, W., et al. 1989, *A&AS*, 79, 1
- Williams, G. A., King, A. R., Uomoto, A. K., & Hiltner, W. A. 1986, *MNRAS*, 219, 809

- Withbroe, G. L. 1971, in *The Menzel Symposium on Solar Physics, Atomic Spectra, and Gaseous Nebulae*, ed. K. B. Gebbie (NBS Spec. Pub. 353), 127
- Wu, C.-C., Panek, R. J., Holm, A. V., Raymond, J. C., Hartmann, L. W., & Swank, J. H. 1989, *ApJ*, 339, 443

Fig. 1.— Line flux ratio diagrams for AM Her stars.

Fig. 2.— Line flux ratio diagrams for DQ Her stars.

Fig. 3.— Line flux ratio diagrams for dwarf novae in quiescence.

Fig. 4.— Line flux ratio diagrams for eclipsing dwarf novae.

Fig. 5.— Line flux ratio diagrams for eclipsing nova-like variables.

Fig. 6.— Line flux ratio diagrams for all “normal” magnetic and non-magnetic CVs. Error bars are suppressed to reduce clutter. Values for TV Col are shown as triangles, FO Aqr as pentagons, Z Cha as squares, OY Car as circles.

Fig. 7.— Line flux ratio diagrams for “weird” CVs. Note change of scale relative to previous figures.

Fig. 8.— Line flux ratio diagram for all CVs. Error bars are suppressed to reduce clutter. Values for “normal” CVs are shown as crosses, GK Per as triangles, V Sge as pentagons, BY Cam as squares, AE Aqr as circles.

Fig. 9.— Model line flux ratio diagram for photoionized thermal emission models. Note that range of x axis differs from previous figure. Symbols are as follows: Model A = ■, Model B = ●, Model C = ×, Model D = +, Model E = □, Model F = ○. Observed line flux ratios for all “normal” CVs are shown as points.

Fig. 10.— Model line flux ratio diagram for photoionized scattering line models. Symbols are as follows: Model A' = ■, Model B' = ●, Model C' = ×, Model D' = +. Observed line flux ratios for all “normal” CVs are shown as points.

Fig. 11.— Schematic model line flux ratio diagram showing U-shaped trajectory.

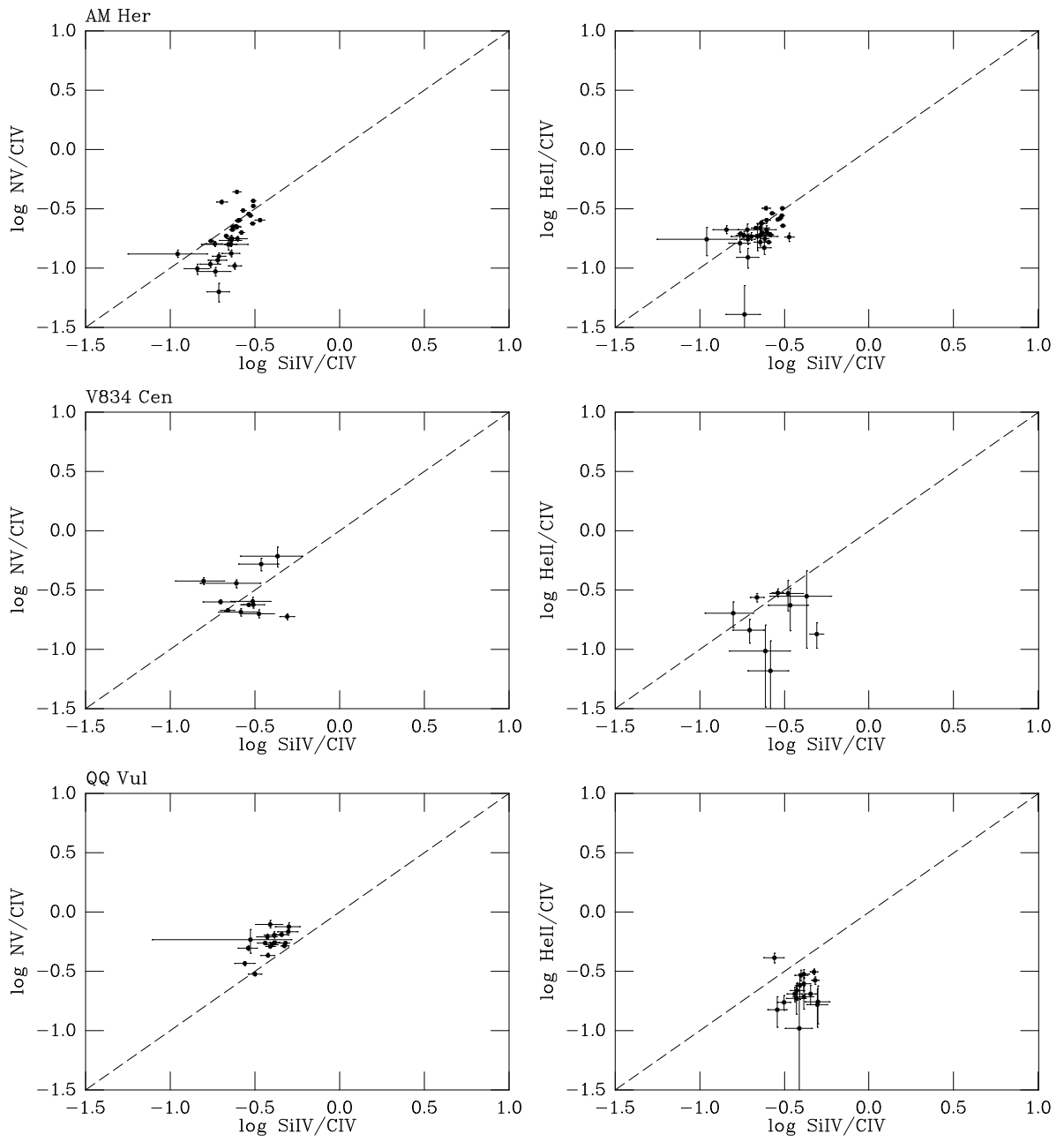


Figure 1

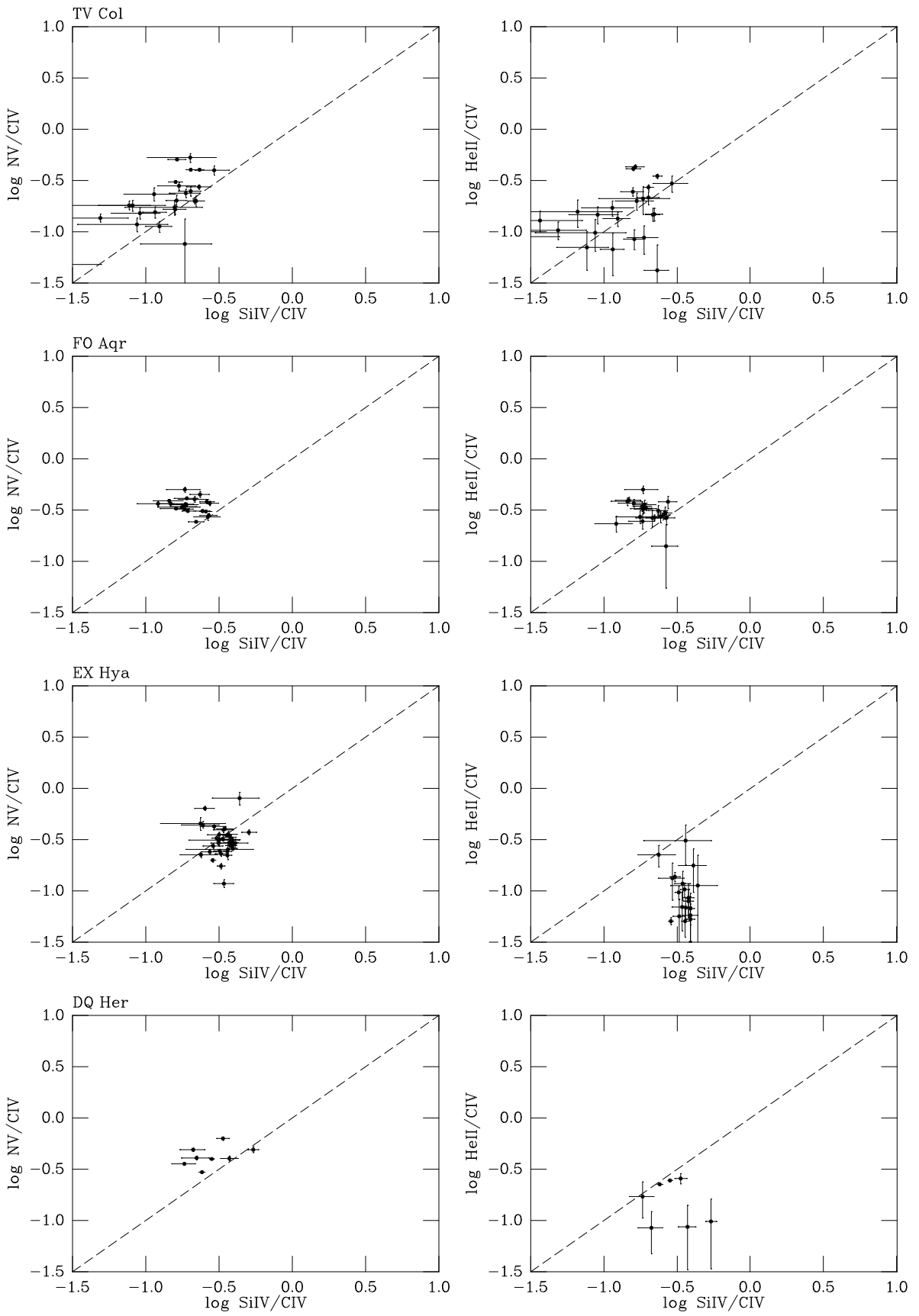


Figure 2

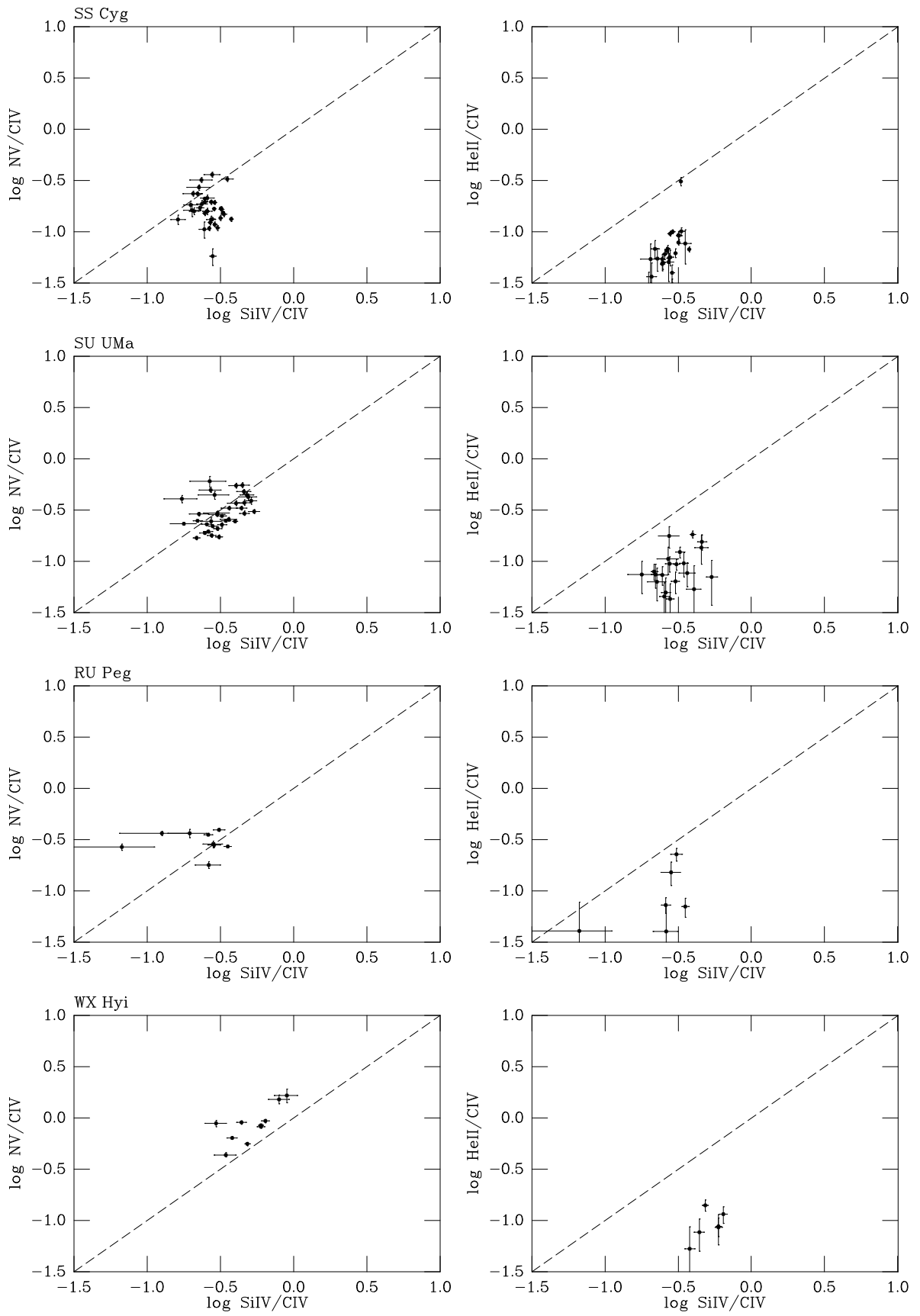


Figure 3

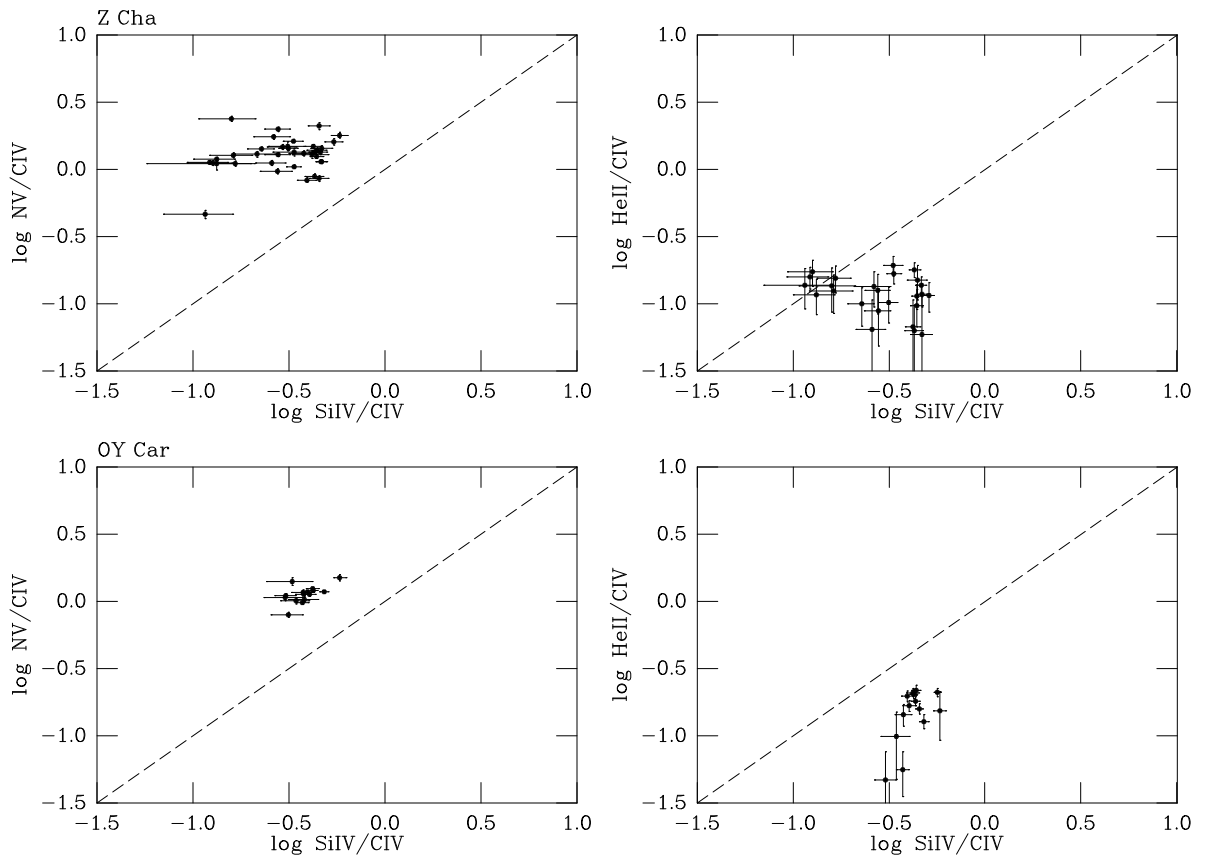


Figure 4

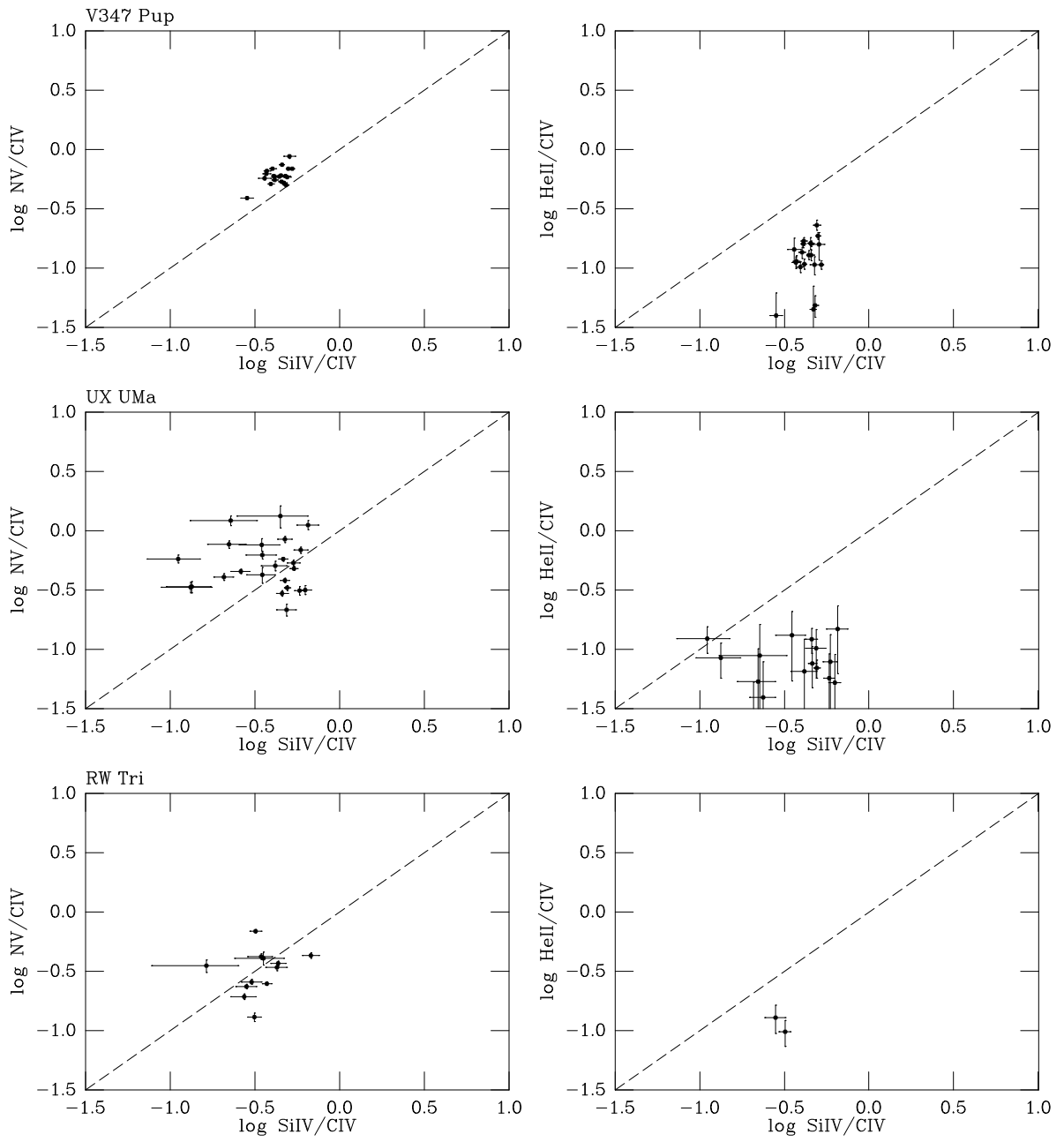


Figure 5

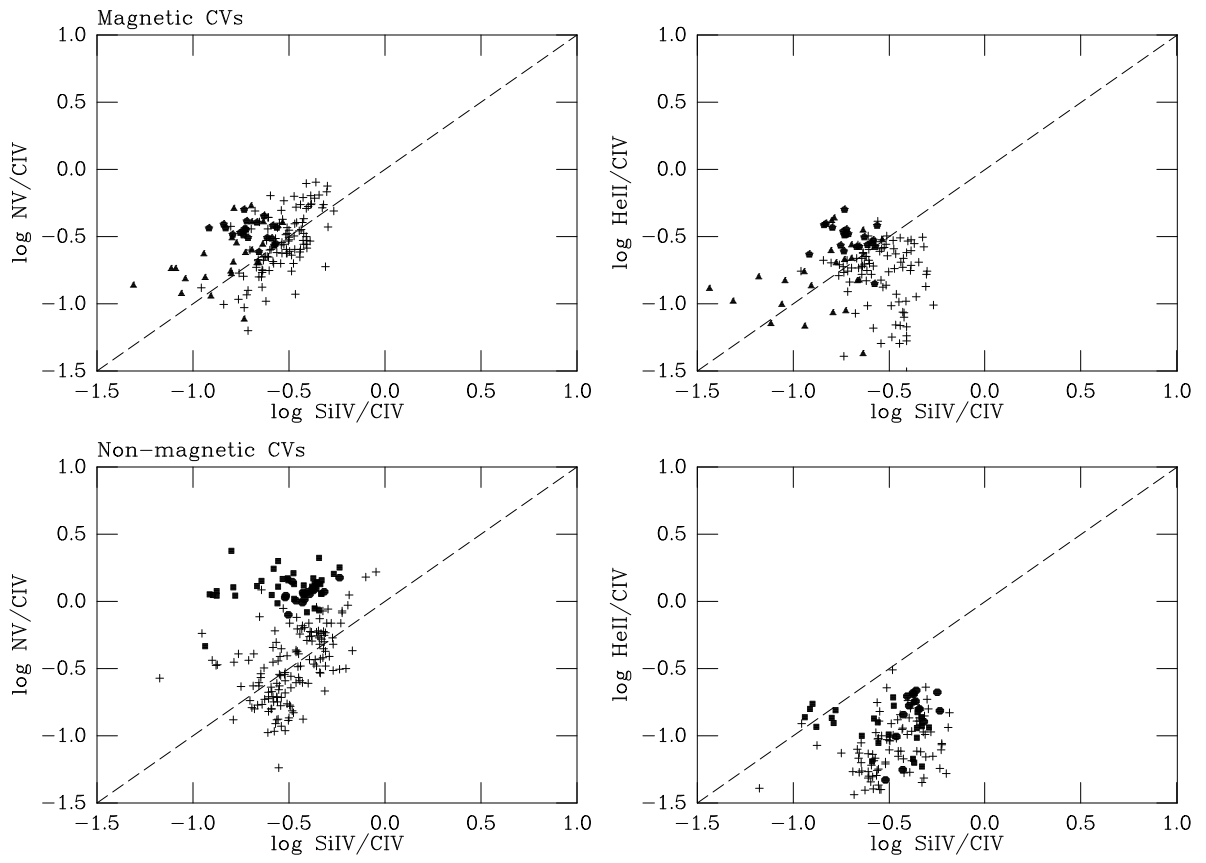


Figure 6

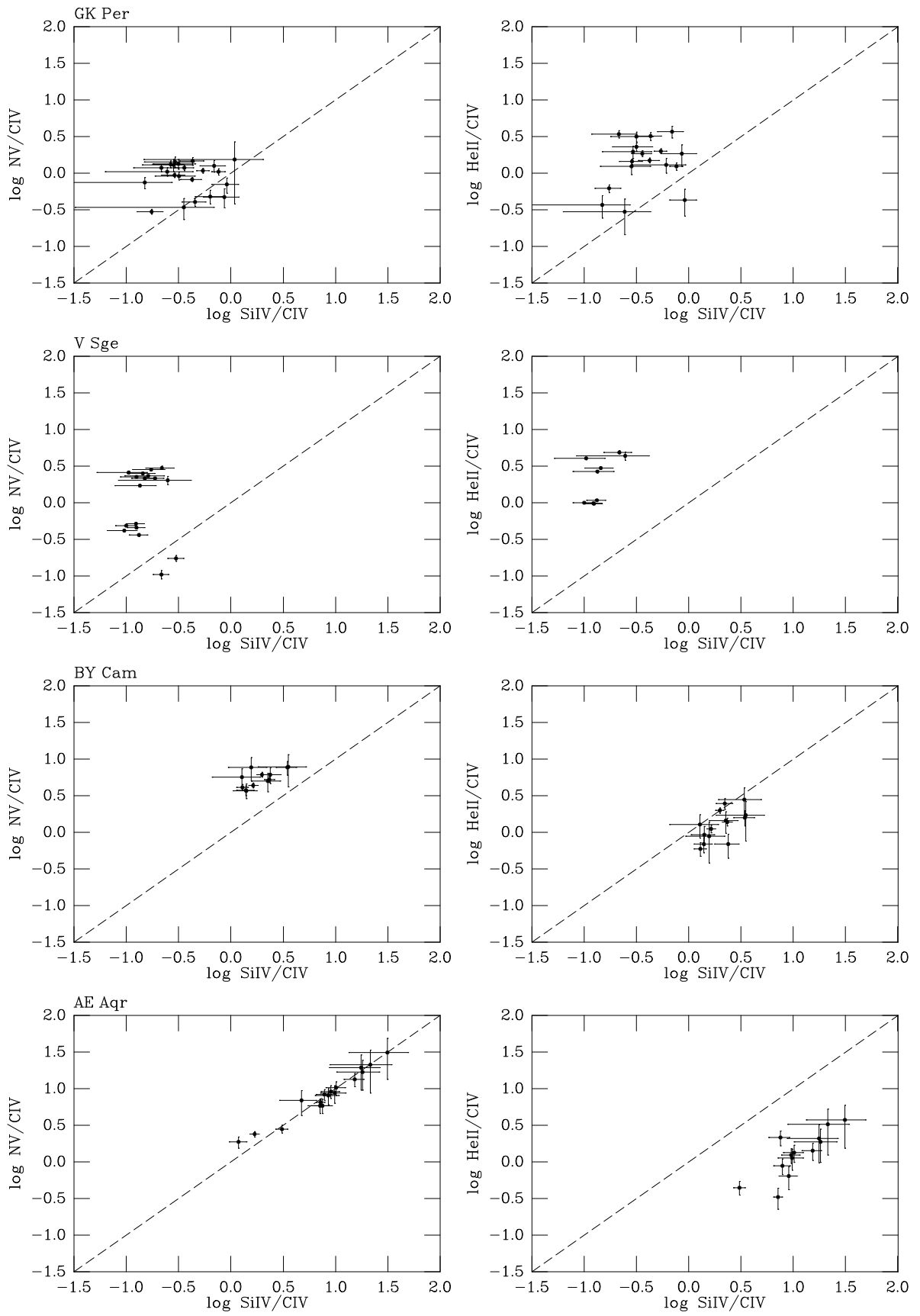


Figure 7

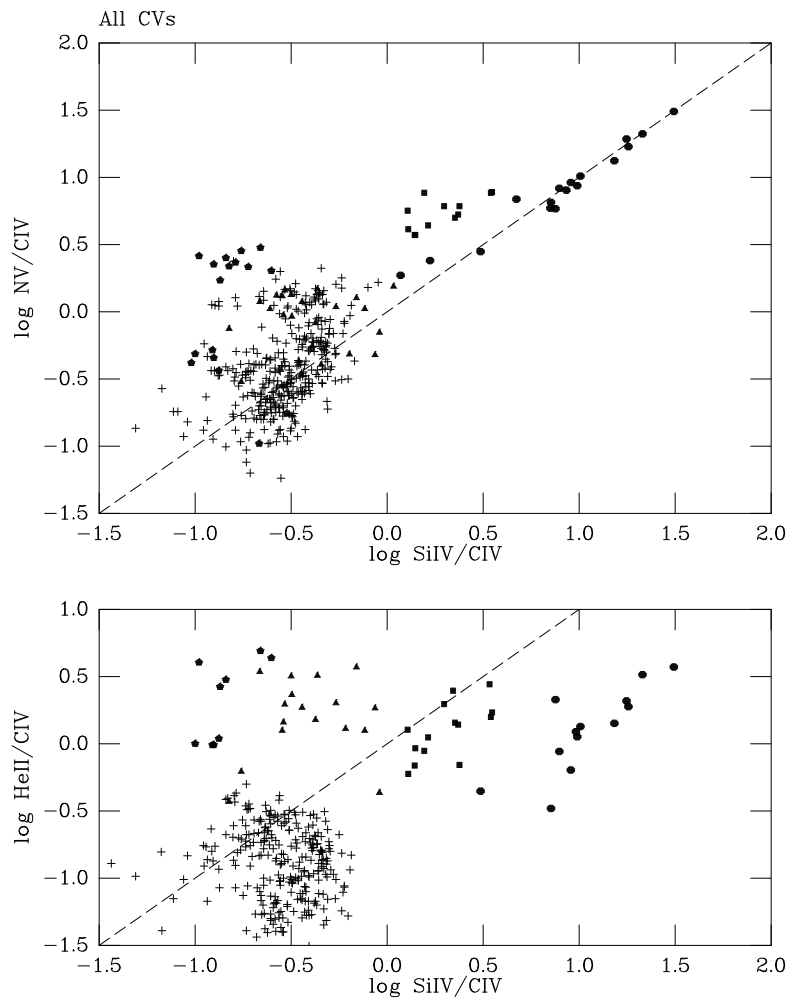


Figure 8

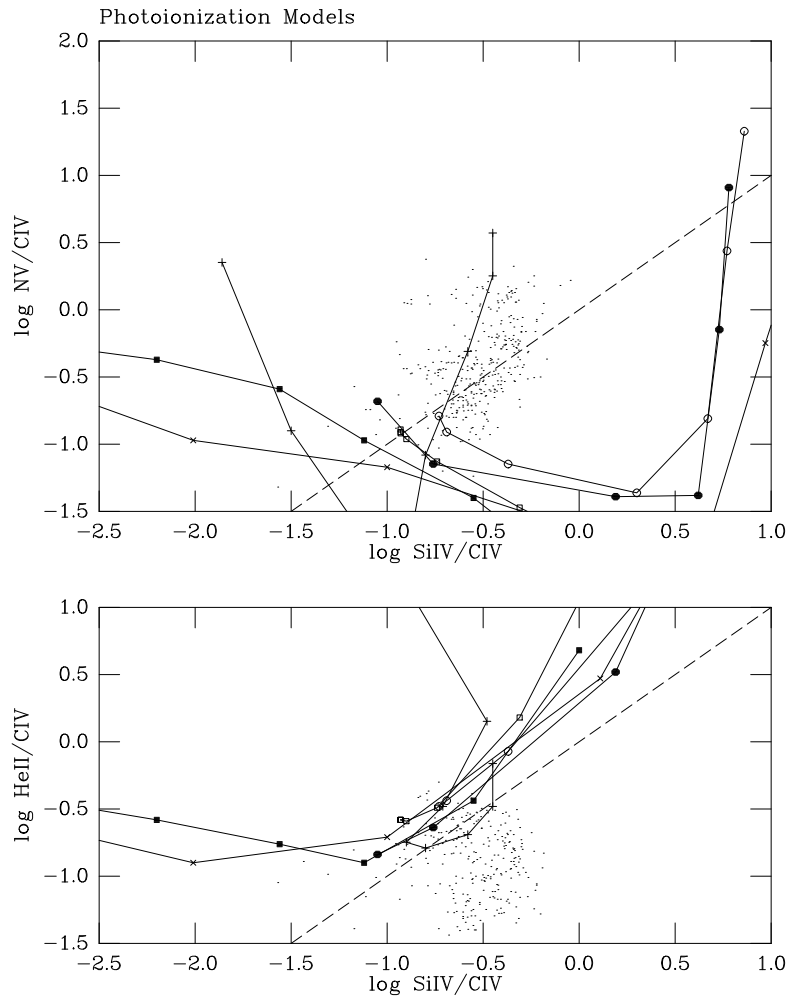


Figure 9

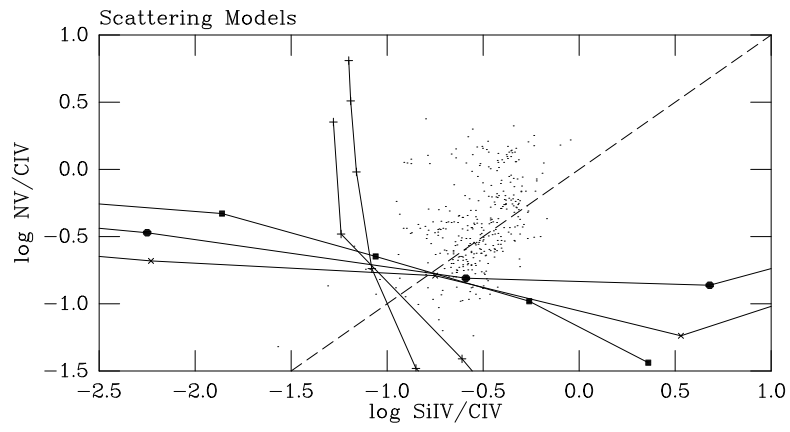


Figure 10

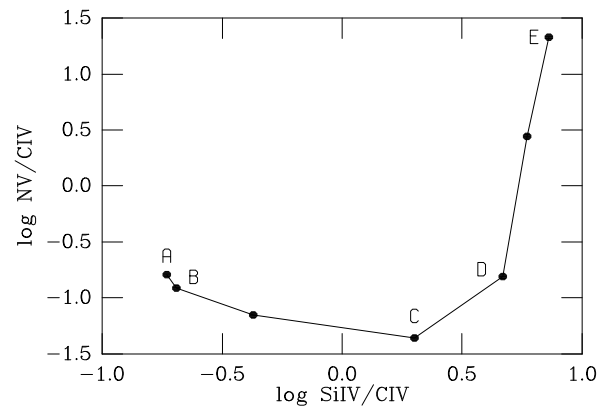


Figure 11